Abnormal Copper Coordination obtained by TiO2 overlayer as a key for enhanced photocatalytic hydrogen generation

Vien-Duong Quach, Maria Chiara Spadaro, Diana Dragoe, Marc Botifoll, Herve Vezin, Christophe Colbeau Justin, Franck Dumeignil, Jordi Arbiol, Robert Wojcieszak, Mohamed Nawfal Ghazzal

▶ **To cite this version:**

Vien-Duong Quach, Maria Chiara Spadaro, Diana Dragoe, Marc Botifoll, Herve Vezin, et al.. Abnormal Copper Coordination obtained by TiO2 overlayer as a key for enhanced photocatalytic hydrogen generation. Journal of Materials Chemistry A, 2024, Journal of Materials Chemistry A, 10.1039/d4ta03072a . hal-04633023

HAL Id: hal-04633023
https://hal.univ-lille.fr/hal-04633023

Submitted on 3 Jul 2024

HAL is a multi-disciplinary open access archive for the deposit and dissemination of scientific research documents, whether they are published or not. The documents may come from teaching and research institutions in France or abroad, or from public or private research centers.

L'archive ouverte pluridisciplinaire **HAL**, est destinée au dépôt et à la diffusion de documents scientifiques de niveau recherche, publiés ou non, émanant des établissements d'enseignement et de recherche français ou étrangers, des laboratoires publics ou privés.

Distributed under a Creative Commons Attribution - NonCommercial 4.0 International License

Check for updates

View Article Online
View Journal

Journal of
Materials Chemistry A

Materials for energy and sustainability

Accepted Manuscript

This article can be cited before page numbers have been issued, to do this please use: V. Quach, M. C. Spadaro, D. Dragoe, M. Botifoll, H. Vezin, C. Colbeau Justin, F. Dumeignil, J. Arbiol, R. Wojcieszak and M. N. Ghazzal, *J. Mater. Chem. A*, 2024, DOI: 10.1039/D4TA03072A.

This is an Accepted Manuscript, which has been through the Royal Society of Chemistry peer review process and has been accepted for publication.

Accepted Manuscripts are published online shortly after acceptance, before technical editing, formatting and proof reading. Using this free service, authors can make their results available to the community, in citable form, before we publish the edited article. We will replace this Accepted Manuscript with the edited and formatted Advance Article as soon as it is available.

You can find more information about Accepted Manuscripts in the Information for Authors.

Please note that technical editing may introduce minor changes to the text and/or graphics, which may alter content. The journal's standard Terms & Conditions and the Ethical guidelines still apply. In no event shall the Royal Society of Chemistry be held responsible for any errors or omissions in this Accepted Manuscript or any consequences arising from the use of any information it contains.

ROYAL SOCIETY OF CHEMISTRY

rsc.li/materials-a

ARTICLE

View Article Online
DOI: 10.1039/D4TA03072A

Abnormal Copper Coordination obtained by TiO_2 overlayer as a key for enhanced photocatalytic hydrogen generation

Received 00th January 20xx,
Accepted 00th January 20xx

DOI: 10.1039/x0xx00000x

Vien-Duong Quach,[a] Maria Chiara Spadaro,[b,g] Diana Dragoe,[d] Marc Botifoll,[b] Hervé Vezin,[f] Christophe Colbeau-Justin,[a] Franck Dumeignil,[e] Jordi Arbiol,[b,c] Robert Wojcieszak,[e] and Mohamed Nawfal Ghazzal,[a†]

Strong metal-support interaction (SMSI) is a pivotal strategy in thermal catalysis, while its application in photocatalysis leaves ample area for further development. A method inducing the SMSI between earth-abundant metals, such as copper and TiO_2, at room temperature, hindering the agglomeration of copper species remains rarely reported. In this work, we achieve SMSI construction of TiO_2 overlayer on Cu nanoparticles via a straightforward soft-chemistry method. The SMSI coverage is even stable after high-temperature treatment in the air (500°C), as demonstrated by chemical mapping and surface analysis. The method is more accurate than thermal reduction since it produces a metastable, highly active anatase phase. Interestingly, the TiO_2 overlayer induces the formation of six-coordinated copper (II) species surrounded by oxygen atoms, resulting in coexisting CuO_2 planes monitored by high-resolution transmission electron microscopy and electron paramagnetic resonance spectroscopy. The stronger interfacial interaction by forming Ti-O-Cu bonding promotes charge carrier separation, producing twice as much H_2 than the low interfacial interaction within a conventional photoactive system wherein copper was decorated onto TiO_2. Our approach offers a rational design for SMSI materials in photocatalysis, extendable to other catalytic reactions.

Introduction

Solar fuel production presents a promising method for converting sunlight into a renewable, sustainable, and environmentally friendly energy source. Hydrogen, a clean fuel generated through solar water splitting, has emerged as a promising solution for climate challenges. H_2 can be produced through three distinct approaches: photocatalytic (PC), photoelectrochemical (PEC), and photovoltaic–electrolysis (PV–EC) routes.[1–3] Although PEC and PV-EC are recognized as advanced solar-to-hydrogen chemical fuel technologies, their scalability requires significant investment, leading to high-cost implications. On the other hand, the photocatalytic process has demonstrated low-cost investment and a promising conversion of solar energy to green hydrogen at the 100 m^2 scale.[4] Since the discovery of the light-induced water splitting reaction over a titanium dioxide (TiO_2) electrode in the 1970s,[5] efforts have been devoted to enhancing its efficiency. While the development of novel nanostructures,[6–8] construction of heterojunctions,[9] induction of oxygen vacancies,[10] or coupling TiO_2 with the promising 2D graphdiyne carbon allotrope,[11] have shown effective improvement in photocatalysis, the most widely adopted strategy involves the surface coupling with metallic nanoparticles. Noble metals, such as Pt, Pd, and Au,[12] generally exhibit the highest photoactivity due to their intrinsic properties. Recent developments have focused on downsizing these cocatalysts from nanoparticles to single atoms, aiming to modify their electronic properties, although this approach has encountered certain bottlenecks. From this perspective, the design and control of the metal-support interface have emerged as novel factors to enhance activity in catalytic reactions, leading to the development of the so-called strong metal-support interaction (SMSI) concept.[15,16] While the SMSI construction is a pivotal strategy in thermal catalysis, its application in photocatalysis leaves ample room for further studies.[17,18] The exploration of the aforementioned MSI phenomena should be extended, as it can lead to a rearrangement of electrons within both materials,[19] favorable separation of photogenerated charge carriers, and modification of the adsorption of H_2O or CO_2.[6,20] Various methods have been proposed to construct a strong metal-support interface, especially at a mild condition, including the mechano-chemistry, soft-chemistry, photoinduced reduction of the support, etc,[21,22] instead of the conventional reductive high temperature conditions (500-700°C). However, most reported studies have demonstrated that the SMSI concept works for VIIIB group metals, and more recently for IB group metal Au,[23,24] with a few studies dedicated to earth-abundant copper metal nanoparticles.[25–27]

In this study, we regulated the interaction between TiO_2 and CuO_2 for photocatalytic hydrogen generation. Copper, and its oxidized forms in general, have become one of the most promising alternatives to noble metals for proton photoreduction. Copper exists in various oxidation states, including Cu^0, Cu^I, Cu^{II}, and Cu^{III}, can exist not only in an exclusive state but also in mixed states involving both zero-valent metals and oxides.[28] Cu^0, $Cu^{(I)}_2O$, and $Cu^{(II)}O$ are typically the most common copper species reported in TiO_2-based photocatalysis.[29,30] Although less explored in photocatalytic

[a] Institut de Chimie Physique, Université Paris-Saclay, CNRS UMR 8000, F-91405 Orsay, France.
[b] Catalan Institute of Nanoscience and Nanotechnology (ICN2), CSIC and BIST, Campus UAB, Bellaterra, ES-08193 Barcelona, Catalonia, Spain.
[c] ICREA, Pg. Lluís Companys 23, ES-08010 Barcelona, Catalonia, Spain.
[d] Institut de Chimie Moléculaire et des Matériaux d'Orsay, Université Paris-Saclay CNRS UMR 8182, F-91405 Orsay, France.
[e] UCCS – Unité de Catalyse et Chimie du Solide, Université de Lille, CNRS UMR 8181, F-59000 Lille, France
[f] LASIRE– Laboratoire avancé de spectroscopie pour les interactions la réactivité et l'environnement, Université de Lille, CNRS UMR 8516, F-59000 Lille, France
[g] Department of Physics and Astronomy "Ettore Majorana", CNR-IMM, University of Catania, via S. Sofia 64, Catania 95123, Italy.
† Email: mohamed-nawfal.ghazzal@universite-paris-saclay.fr
Electronic Supplementary Information (ESI) available: See DOI: 10.1039/x0xx00000x

Open Access Article. Published on 10 June 2024. Downloaded on 6/11/2024 10:14:32 AM.
This article is licensed under a Creative Commons Attribution-NonCommercial 3.0 Unported Licence.

Journal of Materials Chemistry A Accepted Manuscript

View Article Online
DOI: 10.1039/D4TA02073A

Open Access Article. Published on 10 June 2024. Downloaded on 6/11/2024 10:14:32 AM.
This article is licensed under a Creative Commons Attribution-NonCommercial 3.0 Unported Licence.

Journal of Materials Chemistry A Accepted Manuscript

reactions, especially with TiO_2-based photocatalysts, CuO_2 has been reported for fast charge transport, showing great potential in cuprate superconductor engineering, solid-state physics, and cancer treatment.[31–33] Herein, we identify CuO_2 as a highly effective candidate for photocatalytic hydrogen generation. Additionally, tuning the interfacial interaction by constructing a metal oxide-support interface facilitates the transport and prolongs the lifetime of charge carriers that play a pivotal role in photon-to-hydrogen conversion.

Results and discussion

Microstructure and morphology characterization

The interaction between titania and cuprate oxide was regulated using a soft-chemistry method.[6] We impregnated the surface of silica spheres (used as inert support) either with $CuCl_2$ or titania precursor to construct nanostructures: SiO_2@TiO_2@Cu (TiO_2/Cu) and SiO_2@Cu@TiO_2 (MSI-Cu/TiO_2). The details of the synthesis and the aspect of the samples are shown in **Fig. S1**. The microstructure and morphology of the as-synthetized photocatalysts were observed using transmission electron microscopy (TEM) and high-angle annular dark-field scanning transmission electron microscopy (HAADF-STEM) (**Fig. 1A**, **Fig. S2A,** and **Fig. S3A**). The images showed the spherical shape of nanostructures scaffolded using a SiO_2 core. The diameter of the spheres was estimated to be around 200 nm. The SiO_2 microspheres behave as convex nano-lenses, which optimize electromagnetic field enhancement or even lead to an illumination focus point at the front surface of the nanostructure, resulting in optimal light harvesting.[34] High-resolution transmission electron microscopy (HRTEM) shows a TiO_2 anatase phase-structured shell with a thickness of less than 10 nm for SiO_2@TiO_2 (**Fig. S2B**). The thin TiO_2 overlayer was observed to cover copper nanoparticles with a size of 7-10 nm for MSI-Cu/TiO_2 (**Fig. 1B**). The crystal of copper oxide species was assigned to orthorhombic CuO_2 and the indexed Fast Fourier Transform (FFT) patterns of the metallic species clearly showed the presence of the {111} and {110} family planes, noting that the observed structure was oriented along its [110] zone axis. For TiO_2/Cu, we could observe a homogeneous dispersion of copper species and TiO_2 forming a continuous shell around the silica spheres. The HRTEM images in **Fig. S3-B, C** and their corresponding indexed FFT showed that the studied nanoparticle crystallized in the CuO_2 orthorhombic structure with a preferential orientation along the [001] zone axis. From the results, we suspect that the cuprate CuO_2 does not exist separately in such crystalline form. In fact, its coexistence as superconducting CuO_2 planes is evidenced by the abnormal coordination of copper electronic state.[35] This will be clarified by EPR and XPS later.

The crystalline structure was further analyzed using X-ray powder diffraction (XRD), as shown in **Fig. 1F**. Diffractograms exhibited broad peaks at 22°, which correspond to an amorphous SiO_2 core. In addition, characteristic peaks at 25.3° were recorded in the diffraction patterns of samples that identify the lattice plane (101) of TiO_2 anatase phase. Other characteristic peaks of TiO_2 anatase showed up in the patterns, pointing out the presence of their corresponding lattice planes, including (004), (020), (200), (105), and (204). The patterns displayed no trace of cuprate species due to the small size of the nanoparticles and their low quantity as well.

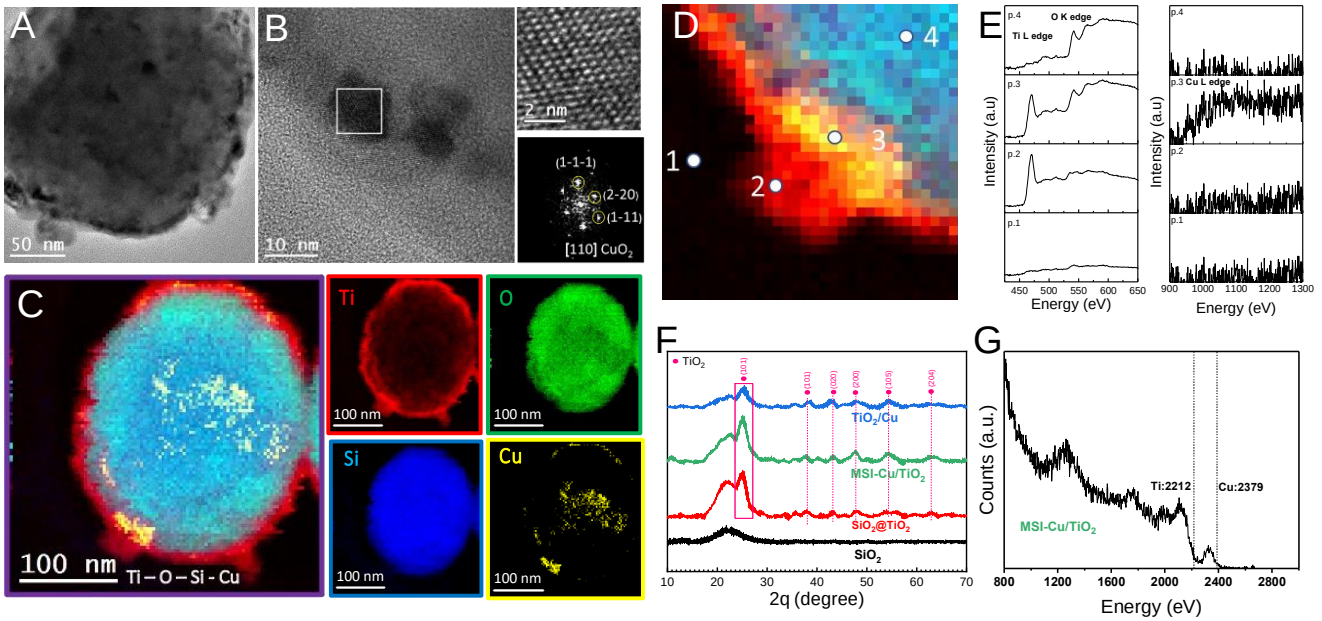

Fig. 1| Microstructure and morphology of photocatalyst. (A) TEM image of MSI-Cu/TiO_2. **(B)** High magnification HRTEM image emphasizing encapsulated cuprate nanoparticle and its index power spectrum. **(C)** EELS-STEM chemical mapping of MSI-Cu/TiO_2 and chemical composition: Ti L edge at 456 eV (scarlet red), O K edge at 532 eV (kelly green), Cu L edge at 931 eV (lemon yellow) and Si K edge at 1839 eV (ultramarine blue). **(D)** Magnified image of EELS-STEM mapping. **(E)** Extrapolated EELS spectra at different regions on the MSI-Cu/TiO_2 surface. **(F)** Powder XRD patterns noted with Miller indices of SiO_2, SiO2@TiO_2, MSI-Cu/TiO_2, and TiO_2/Cu. **(G)** LEIS spectra measured at iso-dose of $1x10^{15}$ He^+ ions.cm^{-2} for MSI-Cu/TiO_2.

This journal is © The Royal Society of Chemistry 20xx

Please do not adjust margins

View Article Online DOI: 10.1039/D4TA02070A

The scanning transmission electron microscopy coupled with electron energy loss spectroscopy (STEM-EELS) provided chemical mapping of different elements (Ti, O, Si, and Cu), hence visualizing their spatial distribution within the nanostructures. **Fig. 1C, S2D,** and **S3-E,F** show that the core of the sphere, mainly consisting of Si and O, was surrounded by a homogeneous TiO_2 overlayer. The EELS obtained within the marked regions in **Fig. 1D** evidence the presence of both Ti L edges (456 eV) and O K edges (532 eV) EELS signals at the shell (regions 2 and 3) and the core surface (region 4). Remarkably, the Ti signal appears in region 3, where the Cu EELS signal was also observed (**Fig. 1E**), demonstrating coverage of the Cu by a TiO_2 overlayer. To further investigate the TiO_2 overlayer and confirm the nature of the CuO_2 coverage, we performed low-energy ion scattering (LEIS) depth profiling spectroscopy. The LEIS reveals information about the composition in the depth of a surface (1-5 nm) by bombarding a sample with noble gas ions of well-defined and low energy at 4.1 x 10^{15} He^+ ions.cm^{-2} (**Fig. 1G**). As the surface is progressively etched by the ion beam, gradients of concentrations from the uppermost layers to the layers below can be inspected. The first recorded signals, at a very low ion dose, were moderate, reflecting the removal of contamination (carbon, hydrogen, etc.) by the ion beam; these species were discarded for analysis. Given the lack of standardization for measurements on nanoparticles distributed over a porous support and the initial presence of contamination layers, translation of the results to a probed depth expressed in nanometre would not be attempted. The presence of Cu atoms in the outer shells of the MSI-Cu/TiO_2 sample was evidenced. However, the signal of Ti was dominant to the ones of Cu and Si, indicating the low quantity of Cu and Si atoms on the surface. In general, LEIS measurements directly confirm the existence of a Cu enrichment in the outer shells of the photocatalyst. It demonstrates that the TiO_2 overlayer partially covers CuO_2 nanoparticles or the thin layer is discontinuous.

Defective surface structure and electronic states

We employed electron paramagnetic resonance spectroscopy (EPR) to analyze the nature of Cu species and hence get information about the oxidation state and coordination of EPR active copper sites (Fig. 2A); the EPR spectrum of SiO_2@TiO_2 as a reference was illustrated in **Fig. S4A**. In detail, Cu^{2+} (d^9) species contain an odd number of electrons assigned to a spin s = 1/2, resulting in an EPR transition. The two principal isotopes of copper (^{63}Cu and ^{65}Cu) have similar nuclear spins of $3/2$, leading to the splitting of Zeeman line into four lines (m_I= $3/2, 1/2, (-1)/2, (-3)/2$).[36–38]. However, only the splitting in the z-direction is large enough to be visualized. The Jahn–Teller distortion is most encountered in octahedral complexes, especially six-coordinate copper(II) species surrounded by oxygen atoms.[39] **Fig. 2A** compared EPR spectra of MSI-Cu/TiO_2 and TiO_2/Cu. In particular, MSI-Cu/TiO_2 photocatalyst exhibited an axial EPR spectrum involving typical parallel and perpendicular edges, revealing two different Cu sites, in agreement with previous studies.[40,41] The hyperfine splitting $A_{//}$ of 122 G at $g_{//}$-factor of 2.402 can be attributed to the charge of donor atoms coordinating to Cu. The splitting by four unveils the presence of Cu^{2+} sites coordinated with four oxygen atoms that attest to the existence of CuO_2 revealed by HRTEM. The partial coverage of TiO_2 onto cuprate nanoparticles could create heterobimetallic sites *via* metal-oxygen-metal support bonding, particularly Ti-O-Cu, leading to the extraordinarily abnormal coordination of Cu^{2+} (crystal structure[42] in **Fig. 2B**). Copper-deposited on TiO_2 observed an

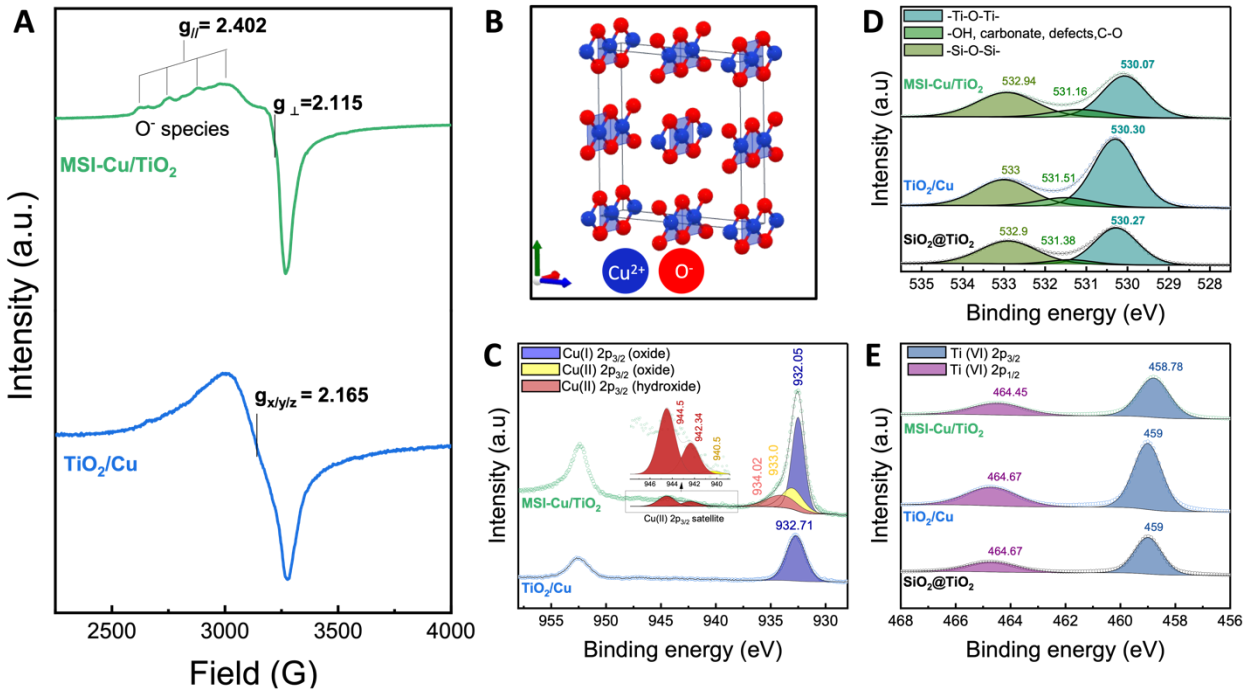

Fig. 2| Characterization of surface electronic properties and catalytic active sites. (**A**) EPR spectra of MSI-Cu/TiO_2 and TiO_2/Cu. (**B**) Crystal structure of cuprate CuO_2. XPS spectra: (**C**) Cu 2p, (**D**) O 1s, and (**E**) Ti 2p.

Open Access Article. Published on 10 June 2024. Downloaded on 6/11/2024 10:14:32 AM. This article is licensed under a Creative Commons Attribution-NonCommercial 3.0 Unported Licence.

Journal of Materials Chemistry A Accepted Manuscript

Please do not adjust margins

View Article Online
DOI: 10.1039/D4TA07078A

isotropic spectrum. The outermost copper species on TiO_2/Cu are generally bound to polar water molecules, which are most likely to coordinate to Cu^{2+}. As a result, EPR spectrum of these hydrated Cu species typically displayed isotropic pattern, which is similar to EPR spectra of aqueous copper complexes such as $[Cu(H_2O)_6]^{2+}$ or $[Cu(H_2O)_5(OH)]^{+}$.[43,44] Besides, g-factor of 2.165 estimated from EPR spectrum of TiO_2/Cu is fully consistent with those, at around 2.16-2.17, of copper on hydrated zeolite.[45,46] In the case of TiO_2/Cu, no such bond between cuprate and titania was detected.

Surface analysis of the photocatalysts was further carried out by X-ray photoelectron spectroscopy (XPS) (**Fig. S4B**), recording signals of core levels Cu 2p, O 1s, and Ti 2p. In **Fig. 2C**, the high-resolution XPS spectra of Cu 2p show the characteristic peaks assigned to Cu $2p_{3/2}$ and Cu $2p_{1/2}$ transitions with satellite peaks. This indicates the existence of Cu(II) state within the MSI-Cu/TiO_2 sample.[47,48] The Cu $2p_{3/2}$ can be deconvoluted into three peaks cantered at 932.05 eV, 933 eV, and 934.01 eV. The peak at 932.05 eV corresponds to $Cu^{(I)}$ oxide, while these peaks at 933 eV and 934.01 eV are indicative of $Cu^{(II)}$ oxide and $Cu^{(II)}$ hydroxide, respectively.[49] The corresponding shake-up satellite peak at 940.5 eV gives rise to $Cu^{(II)}$ oxide, while the others at 942.34 eV and 944.5 eV evidence $Cu^{(II)}$ hydroxide. These $Cu^{(II)}$ 2p transitions shifted toward lower binding energy, and the satellite was much weaker than previous reports.[47,49] In addition, the XPS Cu 2p spectrum of the TiO_2/Cu sample surprisingly revealed a single peak of Cu 2p3/2 without any shake-up satellite, commonly assigned to the $Cu^{(I)}$ state. The oxidation state change of Cu in TiO_2/Cu and the shift towards lower binding energy of $Cu^{(II)}$ in MSI-Cu/TiO_2 can be attributed to the impact of electron bombardment in a high vacuum environment.[50,51] In fact, the electron bombardment can reduce copper species dispersed on the photocatalyst surface from $Cu^{(II)}$ to $Cu^{(I)}$. This effect becomes evident in the case of TiO_2/Cu, where the TiO_2 overlayer did not protect Cu species and were directly exposed to the electron beam. In general, even though copper species in both MSI and conventional nanostructures were found to exist in $Cu^{(II)}$ state, the MSI-encapsulated one observed an apparent discrepancy. The combinatory features of $Cu(OH)_2$ and CuO reflect an abnormal coordination of $Cu^{(II)}$ species in MSI-Cu/TiO_2, resulting in the coexistence of CuO_2 planes, in agreement with the results obtained from HRTEM and EPR.

In the high-resolution XPS spectra of O 1s (**Fig. 2D, Fig. S4C**), the peaks of lattice oxygen show a shift from ~530.3 eV for TiO_2/Cu and SiO_2@TiO_2 to 530.07 eV for MSI-Cu/TiO_2. In fact, the Ti-O-Cu formation creates oxygen vacancies in the interface that negatively charge the surface, and hence causing the shift. Moreover, Cu atoms link to electronegative O atoms in Ti-O-Ti to construct Ti-O-Cu. Consequently, the remaining Ti atoms (Ti^{4+}) are reduced to Ti^{3+} which can be noticed by the intensity of Ti $2p_{3/2}$ shoulder peak at around 457.6 eV (**Fig. S4D).**[53] The high intensity was detected for MSI-Cu/TiO_2 (**Fig. S4D)**. This demonstrates the generation of Ti^{3+} due to the SMSI construction.

We investigated chemical bonds within our photocatalysts through Fourier-transform infrared spectra, and the results are shown in **Fig. S4E**. The broad bands from 3247 cm^{-1} to 3400 cm^{-1} are attributed to the stretching vibration of hydroxyl groups in silanol (Si-OH) moiety and adsorbed water molecules.[54] The deformation vibration mode of O-H bonds is assigned to the band at 1626 cm^{-1}.[54] The bands around 1109 cm^{-1} and 806 cm^{-1} represent the symmetric and asymmetric stretching vibration mode of Si-O-Si bonds, while the band at 953 cm^{-1} can be due to stretching vibration of Si-O-Ti bonds. FTIR spectroscopy is not sensitive enough to discriminate between interfacial Ti-O-Cu and Ti-O-Si.

Optical properties and photoelectrochemical photon-to-current conversion

The optical properties are evaluated using UV-Vis diffuse reflectance spectroscopy (**Fig. S5-A, B**). The reference (SiO_2@TiO_2) exhibited strong absorption at the wavelength of below 400 nm. The absorption bands for MSI-Cu/TiO_2 and TiO_2/Cu shift toward the visible region. The Cu-mediated photocatalysts absorbed wavelength from 400 nm to 500 nm, wherein the absorption of MSI-Cu/TiO_2 showed a larger extent. This is due to the charge transfer from O 2p of TiO_2 to the d-orbitals of Cu.[55] The TiO_2/Cu samples showed a weak absorption band in the range 500-600 nm and much more slightly from 600 nm toward IR, whereas we observed a reverse pattern for MSI-Cu/TiO_2. In fact, the band from 500 to 600 nm could be assigned to the interband absorption of Cu_2O, while the d-d transition of a single electron among $3d^9$ states of Cu^{2+} species is attributed to the broadband from 600 nm toward IR.[51,56] This clearly evidences that Cu^{2+} species exist in MSI-Cu/TiO_2, while a mixed state with a small amount of Cu^{1+} might be found in TiO_2/Cu. We used the Tauc method to estimate the bandgap energy of 3.19 eV, 3.23 eV, and 3.24 eV for MSI-Cu/TiO_2, TiO_2/Cu, and SiO_2@TiO_2, respectively.[57] The 3.24 eV bandgap energy of SiO_2@TiO_2 corresponds to the anatase phase of TiO_2, which is in agreement with HRTEM results and previous studies. A narrower bandgap of the remaining samples can be explained by bandgap alignment between TiO_2 and CuO_x semiconductor composites, which generates the so-called semiconductor heterojunction. In **Fig. S6**, Mott-Schottky plots of SiO_2@TiO_2, TiO_2/Cu, and MSI-Cu/TiO_2 with positive slope intrinsically demonstrated *n-type* TiO_2. Because Cu content is very low and highly dispersed on the surface of nanostructures, we could not witness any effect of *p-type* CuO_x in these Mott-Schottky plots. We then estimated the flat-band potential, which is Fermi level as no band bending, of our photocatalyst samples. Under UV-Vis irradiation, electrons are excited from valance bands to conduction bands within both semiconductors. These photogenerated electrons are injected among TiO_2 and cuprate clusters through photo-induced interfacial charge transfer (IFCT). This resulted in the rising of the Fermi level, from -0.683 V vs. RHE for pure TiO_2 to -0.725 V vs. RHE and -0.875 V vs. RHE for TiO_2/Cu and MSI-Cu/TiO_2 (**Fig. S6**). Obviously, the metal oxide–support interaction could favor interfacial charge transfer between cuprate and TiO_2, evidenced by the largest anodic shift of flat-band potential. The shift also demonstrates the increasing extent of interfacial band bending, which optimizes charge carrier separation.[60] To examine the effect of encapsulation of CuO_2 nanoparticles on the photocatalytic hydrogen evolution reaction (HER), we carried out the electrochemical performance of the HER and OER in K_2SO_4 electrolyte buffered at pH 7 in the presence of argon bubbles. **Fig. 3A** shows that the current density is markedly improved by

Open Access Article. Published on 10 June 2024. Downloaded on 6/11/2024 10:14:32 AM.
This article is licensed under a Creative Commons Attribution-NonCommercial 3.0 Unported Licence.

Journal of Materials Chemistry A Accepted Manuscript

This journal is © The Royal Society of Chemistry 20xx

Please do not adjust margins

View Article Online
DOI: 10.1039/D4TA03072A

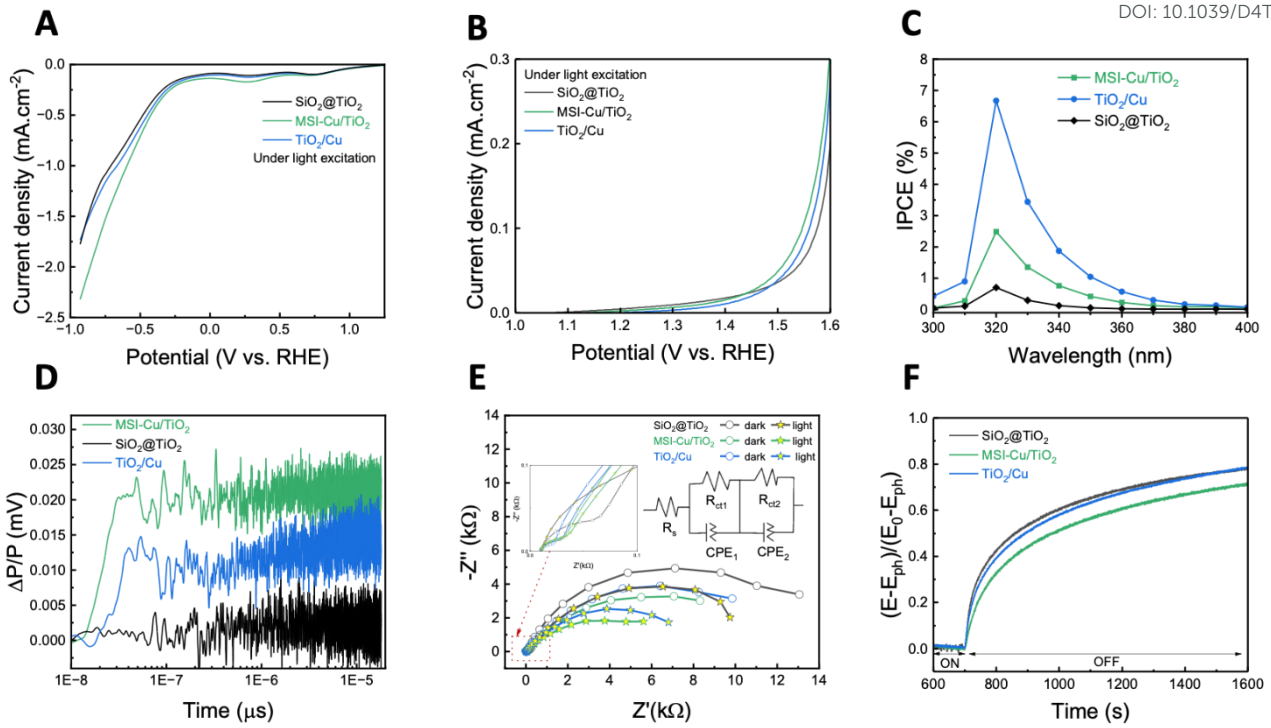

Fig. 3| Photoelectrochemical, and charge carrier dynamics properties of SiO_2@TiO_2, MSI-Cu/TiO_2, and TiO_2/Cu: (**A**) (**B**) Electrochemical activity tests on different photocatalysts in phosphate-buffered K_2SO_4 0.5M electrolyte (pH 7) for the (A) HER and (B) OER through linear sweep voltammetry at scan rate of 0.05 $V.s^{-1}$. **(C)** Incident photon-to-current efficiency (IPCE) spectra in ultraviolet range ran at a fixed bias voltage of 0.6 V vs. Ag/AgCl 3M (~ 1.23 V vs. RHE) in Na_2SO_3 0.1 M buffered at pH = 7 under intermittent illumination triggered from a solar simulator AM 1.5G. **(D)** Time-resolved Microwave Conductivity (TRMC) signals of the samples triggered by laser irradiation (I_{ex}= $6.623\ mJ.cm^{-2}$ at $\lambda = 420\ nm$). **(E)** Electrochemical Impedance Spectroscopy (EIS) Nyquist plots of the front-contact photoelectrodes recorded in dark and AM 1.5G illumination in K_2SO_4 0.5M in the range from 10^{-2} Hz to 100k Hz. **(F)** Normalized open-circuit potential (OCP) decay curves after switching off AM 1.5G solar irradiation.

the encapsulation of Cu and its abnormal coordination. More interestingly, the encapsulation of Cu increases the current density not only in HER but also in oxygen evolution reaction (OER) that MSI-Cu/TiO_2 could be utilized as a photoanode in photoelectrochemical water splitting cell (**Fig. 3B**). The results demonstrate that the intrinsic HER activity can be significantly improved by covering copper by TiO_2 overlayer.

Amperometric photocurrent measurement provided valuable insights into charge carrier mobilities and their trapping within the photocatalysts by examining photocurrent responses (current rise, current decay, etc.). After the light was switched on, photogenerated electron-hole pairs were separated rapidly, charging space charge capacitance. Typically, photocurrent instantaneously rises to a peak value before decaying to a steady state due to electron-hole recombination, accumulation of electrons in bulk or holes on the surface, and trapping of electrons or holes at surface defects.[61] We employed sulfite (SO_3^{2-}) in electrolyte solution to optimize light capture and charge transport. In our case, holding accumulation can be ruled out as a main recombination mechanism thanks to adding sulfite ions as hole scavengers. The higher photocurrent response of TiO_2/Cu reveals the superior separation of photogenerated charge carriers to those in MSI-Cu/TiO_2 and SiO_2@TiO_2 (**Fig. S5C**). While SiO_2@TiO_2 outputted a relatively steady-state photocurrent response, MSI-Cu/TiO_2 and TiO_2/Cu exhibited gradually rising photocurrent curves with no spike. This could be explained by larger depletion layers near the surface or interface of semiconductor-liquid, leading to effective charge carrier separation.

Photocurrent action spectra, including IPCE and APCE under UV and visible illumination (**Fig. 3C** and **Fig. S5-D,E,F**), further examine the photocurrent as a function of the wavelength at an applied bias of 1.23 V vs. RHE. Around 1% of the incident photon at λ = 320 nm was absorbed by SiO_2@TiO_2 photoelectrode to contribute to the photocurrent on the outer circuit. The other 99% was lost due to charge carrier recombination within the material. The external quantum efficiency (IPCE, **Fig. 3C**) was much greater at 2.5 % for MSI-Cu/TiO_2 and nearly 7% for TiO_2/Cu. When considering only charge carrier recombination as a main effect on photocurrent response, we estimated the internal quantum efficiency (APCE, **Fig. S5E**) at over 5% for MSI-Cu/TiO_2 and 9% for TiO_2/Cu. Cu-modified photocatalysts converted visible photons to current despite a negligible extent, while SiO_2@TiO_2 was unactive in the visible range (**Fig. S5-D,F**). These experimental outputs are consistent with the one of UV-vis DRS and amperometric photocurrent response measurements.

We investigated charge carrier dynamics at microsecond and nanosecond timescales by time-resolved microwave conductivity spectroscopy (TRMC) and time-resolved photoluminescence spectroscopy (TRPL). **Fig. S7A** displays TRMC spectra of three photocatalysts triggered by an ultraviolet laser at 360 nm, where TiO_2 is activated only. In detail, the signal of SiO_2@TiO_2 observed the highest maximum intensity and a

Open Access Article. Published on 10 June 2024. Downloaded on 6/11/2024 10:14:32 AM.
This article is licensed under a Creative Commons Attribution-NonCommercial 3.0 Unported Licence.

Journal of Materials Chemistry A Accepted Manuscript

Please do not adjust margins

View Article Online
DOI: 10.1039/D4TA03072A

Table 1| Parametres obtained from EIS, Mott-Schottky, and OCP decay measurements.

Samples		[a]R_{ct2} (Ω)	[b]E_{fb} (V_{RHE})	[c]k_r (s^{-1})
SiO_2@TiO_2	light	11722	-0.683	1×10^{-6}
	dark	14510		
TiO_2/Cu	light	8465.8	-0.725	2.5×10^{-7}
	dark	13022		
MSI-Cu/TiO_2	light	6826.6	-0.875	1.9×10^{-8}
	dark	11175		

[a]R_s, R_{int}, R_{ct} were estimated by EIS plot fitting. [b]E_{fb} values were determined from **Fig. S6**. [c]k_r was obtained by fitting OCP curves in **Fig. S7C**.

sharp decay, while MSI-Cu/TiO_2 outputted two times smaller maximum intensity but a long-lasting signal. In fact, electrons, the primary mobile charge carriers in TMRC,[61] were generated in bulk and then transferred to the surface of TiO_2. The sharp TRMC decay of SiO_2@TiO_2 reflects the disappearance of electrons, which could be attributed to electron-hole recombination or surface trapping. Coupling TiO_2 with cuprate nanoparticles induces surface defects, including oxygen vacancies and Ti^{3+}, which are trapping sites.[61] Although the trapping hinders electron transport within the crystalline structure, it precludes electron-hole recombination, leading to a longer charge carrier lifetime. Surprisingly, we recorded the TMRC signal of TiO_2/Cu at a much lower maximum intensity. These results suggested that less surface defects are created in this system. We recorded the TRMC signal under visible laser excitation (λ_{ex}=420 nm), activating only cuprate oxide. As a result, in **Fig. 3D**, the TRMC signal of SiO_2@TiO_2 displayed flat fluctuation at 0 mV, while those of the composites showed higher charge density and an unexpectedly longer lifetime. The visible laser generates charge carriers, mainly electrons, within the CuO_2 band structure. These electrons are injected into the conduction band of TiO_2, while holes are accumulated into the valence band of CuO_2. This inhibits charge carrier recombination and thus prolongs charge carrier lifetime, as evidenced by non-decayed TRMC signals. TRPL spectroscopy further elucidated charge carrier dynamics at nanosecond timescale *via* inspecting photons released from the relaxation of photogenerated charges. Time-resolved photoluminescence (TRPL) in **Fig. S7B** exhibited the sharpest decay with respect to MSI-Cu/TiO_2, followed in order by the one of TiO_2/Cu and SiO_2@TiO_2. The high probability of electron-hole recombination within SiO_2@TiO_2 would be responsible for its slighter TRPL decay. In the case of TiO_2/Cu and MSI-Cu/TiO_2, non-irradiated relaxation of electrons, such as electron trapping and transfer, are more favorable, leading to sharper TRPL decay. These experimental results are consistent with the TRMC analysis.

The charge transport capability in the CuO_2/TiO_2 interface was studied by electrochemical impedance spectroscopy (EIS). The data was fitted to an equivalent circuit model (inset **Fig. 3E**) involving two parallel branches (R_{ct1} and CPE_1) derived from the interfacial contact between FTO and semiconductive materials. R_{ct2} and CPE_2 represent charge transfer resistance and double-layer capacitance, respectively, at the electrode and electrolyte interface, and R_s stands for Ohmic resistance. To address electrochemical phenomena on a non-uniform surface, it is essential to incorporate constant phase elements (CPE) with an ideality factor (n) to characterize double-layer capacitance and/or coating capacitance rather than relying on ideal capacitors. Nyquist plots were obtained from electrochemical impedance spectroscopy (EIS) measurements in both dark and under UV-visible irradiation, employing a K_2SO_4 0.5M electrolyte solution. The first compact semicircles (inset **Fig. 3E**) might be due to the interfacial contact between FTO glass electrode and our photocatalysts. The second larger semicircle typically translates the charge transfer impedance between photoelectrode and electrolyte. SiO_2@TiO_2 registered the largest values of charge transfer resistance, followed by TiO_2/Cu, and the smallest values belong to MSI-Cu/TiO_2 (**Table 1**). The result reveals that charge transport is more favorable for CuO_2/TiO_2 composites. Moreover, the low value of charge transfer resistance on MSI-Cu/TiO_2 demonstrates that strong metal oxide-support interaction efficiently contributes to the charge carriers' transfer and separation. Upon illumination condition, the composites became more inductive, evidenced by the smaller diameter of Nyquist semi-circles. This can be ascribed to the abnormal Cu coordination that facilitates charge transfer.

Open-circuit potential (OCP) decay analysis offers information about surface recombination between trapped electrons and reaction intermediates. In fact, the charge carrier recombination occurs at nanoseconds or microseconds timescale, while OCP decay takes several minutes. Open-circuit voltage (V_{OC}) is the difference in Fermi level between a photoelectrode and a counter electrode. Upon illumination, photogenerated electrons fill up the Fermi region and shift the Fermi level toward anodic potentials. Following this, the recombination of photogenerated charge carriers occurs and maintains equilibrium with their accumulation at the interface, resulting in a steady state of V_{OC}. When switching the light off, V_{OC} decays upon recombination process due to a lack of charge carrier generation. The normalized transient decay profiles of OCP are illustrated in **Fig. 3F**. The results demonstrate that MSI-Cu/TiO_2 exhibited the most gradual OCP decay, indicating low surface recombination of charge. An average recombination rate constant k_r can be estimated by fitting the OCP decay profile with a pseudo-first-order kinetic model equation[62]:

$$\frac{E - E_{ph}}{E_0 - E_{ph}} = 1 - e^{-k_r t}$$

Open Access Article. Published on 10 June 2024. Downloaded on 6/11/2024 10:14:32 AM.
This article is licensed under a Creative Commons Attribution-NonCommercial 3.0 Unported Licence.

Journal of Materials Chemistry A Accepted Manuscript

This journal is © The Royal Society of Chemistry 20xx

Please do not adjust margins

View Article Online DOI: 10.1039/D4TA03078A

where E is OCP at any time (V), E_0 is the stationary OCP in dark, E_{ph} is the stationary OCP under illumination, k_r is pseudo first-order recombination rate constant (s^{-1}). In this study, we performed fitting decay curves in Matlab (**Fig. S7C**); the corresponding value of the recombination rate constant was listed in **Table 1**. In detail, the recombination rate of MSI-Cu/TiO_2 is around 50 times and 13 times smaller than that of SiO_2@TiO_2 and TiO_2/Cu, respectively. This outcome evidences the role of abnormal Cu coordination induced by strong metal oxide-support interaction in enhancing charge carrier separation within the photocatalyst.

Photocatalytic hydrogen production

The photocatalytic activity of photocatalysts was evaluated following the accumulated hydrogen produced under UV-visible light illumination from methanol/water solution (1:3 v/v). We employed X-ray Fluorescence spectrophotometry (XRF) to quantify the mass percentage of either elements (Si, Ti, O, Cu) or oxides (SiO_2, TiO_2, CuO_x) in our powder samples. Notably, the insulting SiO_2 occupies approximately 85 wt.% while the remaining active phase (TiO_2 and CuO_x), which is involved in photocatalytic reactions, accounts for 15% wt. As a result, we refined the photocatalytic H_2 evolution rate based on the mass percentage of the active phase. As shown in **Fig. 4A**, MSI-Cu/TiO_2 exhibited the highest yield of photocatalytic hydrogen production, reaching nearly 60 mmol.g^{-1} after 5 hours of UV-Vis irradiation. The amount of H_2 generated was approximately twice lower (35 mmol.g^{-1}) for TiO_2/Cu, and only a negligible amount of H_2 was obtained in the sample without CuO_2. Undoubtedly, the synergistic combination of TiO_2 and CuO_2 significantly enhanced the photocatalytic activity for the H_2 generation reaction. This is in line with the enhancement of charge carrier separation and lifetime, as corroborated by PEC results, and despite TiO_2/Cu demonstrating superior absorbed photon-to-current efficiency, evidenced by IPCE and APCE, MSI-Cu/TiO_2 outperformed others in terms of overall photocatalytic

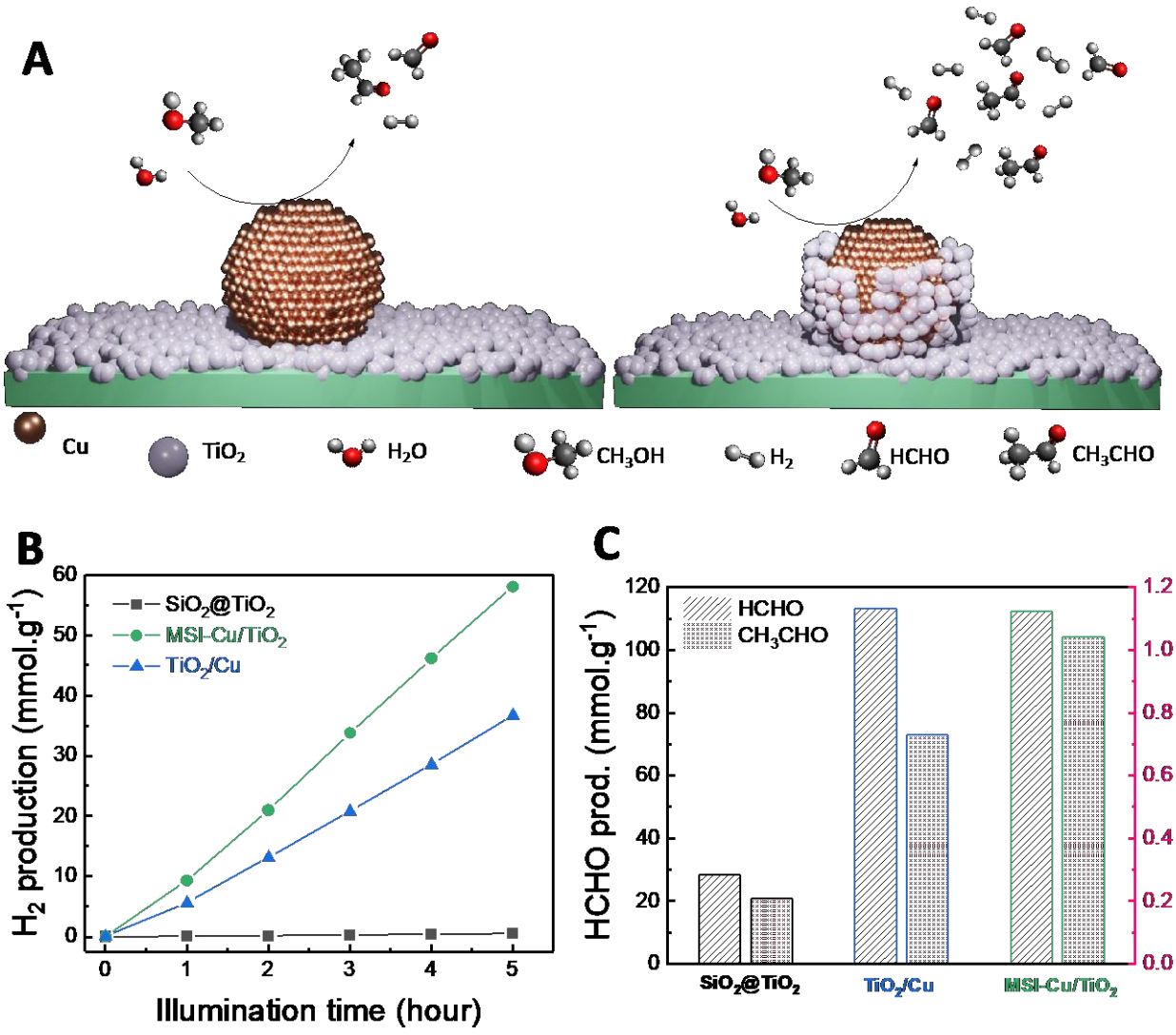

Fig. 4| Photocatalytic activity of SiO_2@TiO_2, MSI-Cu/TiO_2, and TiO_2/Cu: (A) Graphic illustration of photocatalytic reactions occurring on TiO_2/Cu and MSI-Cu/TiO_2 photocatalysts. **(B)** Hydrogen production investigated by gas chromatography. **(C)** Formaldehyde and acetaldehyde production investigated by high performance liquid chromatography. Reaction conditions: 10 mg/10 mL photocatalyst, 25°C, H_2O:CH_3OH = 3:1 v/v, UV-Visible irradiation Mercury lamp 150W.

Open Access Article. Published on 10 June 2024. Downloaded on 6/11/2024 10:14:32 AM. This article is licensed under a Creative Commons Attribution-NonCommercial 3.0 Unported Licence.

Journal of Materials Chemistry A Accepted Manuscript

Please do not adjust margins

View Article Online
DOI: 10.1039/D4TA02670A

Open Access Article. Published on 10 June 2024. Downloaded on 6/11/2024 10:14:32 AM.
This article is licensed under a Creative Commons Attribution-NonCommercial 3.0 Unported Licence.

Journal of Materials Chemistry A Accepted Manuscript

efficiency. This superiority is closely linked to the charge carrier dynamics within the nanostructures, which are pivotal in improving photocatalytic activity. The observed color change during the photocatalytic reaction of MSI-Cu/TiO_2 from greenish to dark red testifies to a change in the oxidation state of Cu (**Fig. S8B**). Indeed, some photogenerated electrons could be promoted from TiO_2 to unoccupied d^9 orbitals of Cu^{II}, resulting in a fulfilled d^{10} state of Cu^{I}. More interestingly, the MSI-Cu/TiO_2 turned back to its original greenish color, without air exposure, when illumination was cut off, reflecting the release of the photoelectrons from cuprate to TiO_2. However, TiO_2/Cu displayed no color change, demonstrating a less effective change in the oxidation state of Cu. The partial coverage of TiO_2 onto CuO_2, practicing strong metal oxide-support interaction, generates a significant number of active sites for photocatalytic reactions, thereby enhancing the overall reaction yield. A 20-hour photocatalytic cycling experiment was performed to evaluate the stability of the MSI encapsulation layer and TiO_2/Cu sample. As shown in **Fig. S8A**, a decrease in the amount of H_2 produced is observed for both samples. The H_2 generation decreased by 15% for both systems in the second cycle. The decrease is mainly due to the loss of part of the sample during the recovery by centrifugation. Indeed, after the second cycle, a decrease in H_2 generation is still observed for SMSI (~10%), while TiO_2/Cu shows relatively good stability. After the third cycle, the SMSI system shows relatively good stability and remains more efficient in H_2 generation than TiO_2/Cu (**Fig. S8A**).

The photoactivation mechanism and H_2 generation over the MSI-Cu/TiO_2 sample is depicted in **Fig. 5**. Under light excitation, electrons, and holes are generated in the conduction and valence bands of TiO_2, respectively. Photogenerated electrons are transferred to copper, resulting in the reduction of Cu(II) to Cu(I), as evidenced by the change of the sample's color from green to rust color (dark red) **(Fig. S8B)**. The protonation at TiO_2 overlayer active sites consumes electrons and induces a building field that induces the diffusion of scavenged electrons at d-orbitals of Cu back to the TiO_2 conduction band. When UV-visible illumination was cut off, the electrons at Cu sites were released back to ensure charge balance within the band structure; this was observed by the reversion to the original sample color as well as the oxidation of Cu(I) to Cu(II). In the case of holes, they are scavenged by the sacrificial electron donor molecules (methanol).

To explore the photocatalytic H_2 generation pathway, we extended our investigation to trace intermediates produced during illumination in the liquid phase. Following five hours of illumination, reaction solutions were extracted and injected into a high-performance liquid chromatography (HPLC) – ultraviolet-visible spectroscopy detector. Formaldehyde (HCHO) and acetaldehyde (CH_3CHO) were detected in the liquid phase; HCHO was identified as a primary product from photocatalytic methanol reforming reactions. The production yields of these intermediates were visualized in **Fig. 4C**, where SiO2@TiO2 exhibited the smallest production yield of HCHO compared to the cuprate-mediated samples. This result points out the low kinetic conversion of CH_3OH to HCHO. TiO_2/Cu exhibited a slightly greater extent of the HCHO/CH_3CHO ratio than MSI-Cu/TiO_2. The dissociative adsorption of MeOH, right after the e^-/h^+ generation, leads to the formation of HCHO, followed by the release of H^+. In particular, CH_3OH molecules convert to methyl hydroxyl radicals ($^{\bullet}CH_2OH$) through C-H activation. Then, radicals react with oxidative holes and produce formaldehyde (HCHO). Hydrogen ions generated during reactive transformation would capture photogenerated electrons and combine to release H_2 molecules. MSI-Cu/TiO_2

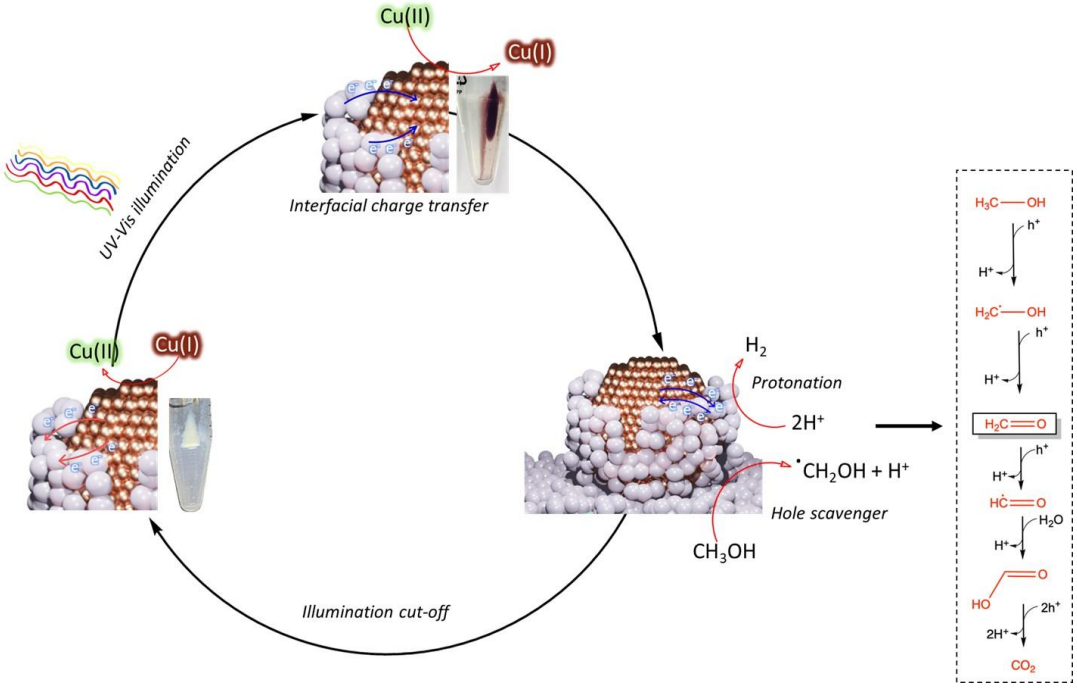

Fig. 5| A schematic illustration of the photocatalytic hydrogen production mechanism with electron transfer pathways and the change in valance state of copper on MSI-Cu/TiO_2

This journal is © The Royal Society of Chemistry 20xx

Please do not adjust margins

View Article Online
DOI: 10.1039/D4TA03972A

Open Access Article. Published on 10 June 2024. Downloaded on 6/11/2024 10:14:32 AM.
This article is licensed under a Creative Commons Attribution-NonCommercial 3.0 Unported Licence.

Journal of Materials Chemistry A Accepted Manuscript

generated higher production of CH_3CHO than TiO_2/Cu, probably due to more likely accessibility of O_{vac} and Ti^{3+} on the surface in the TiO_2 surface facilitated by the abnormal Cu coordination that fastened the photocharges transfer. Although converting CH_3OH to HCHO is more efficient for TiO_2/Cu than MSI-Cu/TiO_2, the H_2 evolution yield for MSI-Cu/TiO_2 was remarkably greater. In the case of TiO_2/Cu, the active sites are likely in the vicinity of the CuO_2-TiO_2 interface, which is typically associated with steric hindrance and low charge transfer. To address this limitation and enhance the kinetic of HCHO oxidation reactions, the position of CuO_2 and TiO_2 could be switched, promoting strong oxide-support interaction through partial encapsulation.

Conclusions

In this study, we present a soft-chemistry approach to construct composite photocatalysts, wherein a TiO_x shell encapsulates highly dispersed CuO_2 nanoclusters on a SiO_2 core. The fine structure was characterized by transmission electron microscopy (TEM, HRTEM, STEM), in combination with EELS chemical mapping and LEIS, which confirmed the partial coverage of TiO_2 onto copper metallic species. Surface analysis through EPR and XPS highlighted the existence of Cu sites coordinated with four oxygen in the case of MSI-Cu/TiO_2. Compared to conventional TiO_2/Cu, it exhibited a superior photocatalytic yield in the hydrogen evolution reaction. We demonstrated optimal charge carrier dynamics and photon-to-current conversion efficiencies within the SMSI-like nanostructure MSI-Cu/TiO2 using photoelectrochemical measurements and time-resolved spectroscopy techniques. In addition, the results underscore the dominance of charge carrier dynamics in driving photocatalytic enhancement.

Experimental

Photocatalyst preparation

Synthesis of monodispersed SiO_2 microspheres. Silica microspheres with a 150-200 nm diameter were synthesized following the Stöber method[63]. A mixture of 42 mL of EtOH and 35 ml of distilled water was stirred in a borosilicate bottle for 10 minutes at room temperature before adding 15 mL of NH_4OH 28% to adjust pH. Once the temperature had been raised to 40°C, 4 mL of TEOS was pipetted to the bottle; the mixture remained stirring for 1h. After that, the white precipitate was centrifugated, washed 3 times with distilled water, and dried at 70°C overnight.

APTMS functionalization. To deposit metal nanoparticles onto the SiO_2 surface, we employed APTMS as a coating agent; 300 mg of SiO_2 beads were then dispersed in 10 mL of EtOH. Next, 0.1 mL of APTMS was added to the mixture under stirring. After six hours of stirring, the APTMS-functionalized SiO_2 was centrifuged and washed with EtOH. The functionalization process was repeated for SiO_2@Cu and SiO_2@TiO_2 before coating with a TiO_2 shell and metallic nanoparticles.

Synthesis of Cu nanoparticles to obtain SiO_2@Cu or SiO_2@TiO_2@Cu. APTMS-functionalized SiO_2 or SiO_2@TiO_2 was dispersed in a solution containing the desired amount of $CuCl_2.2H_2O$ in a round-bottom flask. The volume of the mixture was adjusted to achieve a Cu^{2+} concentration of 0.1M. After sonication for 1 hour, the mixture was purged with Ar for one additional hour and heated to 80°C. Then, 0.82 M of ascorbic acid was added dropwise to the flask at 2 drops per second while vigorously stirring, ensuring a final concentration of 0.4M. The system was heated for an additional 30 minutes after all the ascorbic acid was added. The mixture was cooled to room temperature, and the pH was adjusted to 8 using tetramethylammonium hydroxide. After overnight stirring, the resulting solid was centrifuged, washed thoroughly with H_2O, and dried at 70°C overnight.

Coating cores with TiO_2 thin shell. SiO_2@Cu and SiO_2 cores were coated with a TiO_2 shell through the hydrolysis of TTiP in basic media. In detail, the core nanoparticles were firstly dispersed in 20 mL of EtOH and 0.5 mL of H_2O. Next, this pH was adjusted at 12.4 by adding 0.3 mL of NH_4OH 28%, followed by stirring for 20 minutes. Concurrently, 1.5 mL of TTiP was dissolved in 50 mL of absolute EtOH. This mixture was dropped slowly to the basic solution containing core nanoparticles under stirring at room temperature. After two hours of aging, final core-shell nanocomposites were obtained by centrifugation, then washed carefully with absolute EtOH, and finally dried at 70°C overnight. The photocatalysts need to be calcinated at 500oC for 2 hours at a temperature elevation speed of 2°C/minute.

(Photo)electrochemical measurements

Photoelectrochemical measurements and electrochemical impedance analysis, including amperometry transient photocurrent (TPC), electrochemical impedance spectroscopy (EIS), Mott-Schottky, and open-circuit voltage decay, were carried out in a three-electrode electrochemical cell with/without illuminating by AM 1.5G solar simulator. Photoelectrodes were fabricated by drop-casting 100μL of an ultrasonicated solution (2mg.mL^{-1}) of our samples on fluorine-doped tin oxide-coated glass slides of 2.5 cm^{-2} (FTO glass) before drying overnight at room temperature. The electrochemical setup involved a platinum disk counter electrode and an Ag/AgCl (saturated KCl) reference electrode. The values of potential vs. Ag/AgCl were converted to those vs. RHE through the following equation:

$$E_{R.H.E} = E_{Ag/AgCl} + 0.197 + 0.059 \times pH$$

Experiments were manipulated by potentiostat PGSTAT101 Metrohm Autolab. An open-circuit voltage decay fitting was executed using the inverse method on Matlab. When the numeric and experimental curves show superimposition, the fitting is reliable for estimating important parameters such as the recombination rate constant.

Photocatalytic hydrogen evolution tests

The photocatalytic activity of our photocatalyst was evaluated *via* a hydrogen evolution reaction. Reaction conditions remained identical: the amount of photocatalyst at 10 mg/10 mL, room temperature, and testing duration of five hours under

View Article Online
DOI: 10.1039/D4TA03072A

UV-visible irradiation triggered by a Mercury lamp (150W). Reactors were degassed by argon for 20 min to remove dissolved oxygen completely before illumination. Gaseous products were quantified by the Agilent 990 micro gas chromatography (GC) system facilitated with a thermal conductive detector (TCD). Liquid phase products were detected by high-performance liquid chromatography (HPLC) on Agilent 1260 Infinity with a UV-Vis detector.

Author Contributions

V. D. Quach carried out and set up the design of the experiments and investigation process, data curation, wrote the initial draft, and reviewed and edited the final manuscript. M. C. Spadaro, M. Botifoll, and J. Arbiol performed the electron microscopy analyses and discussed their results. D. Dragoe performed XPS measurements and discussed the results. R. Wojcieszak, H. Vezin, and F. Dumeignil carried out LEIS and EPR; R. Wojcieszak discussed the LEIS result. C. Colbeau-Justin instructed V.D.Quach in TRMC. M. N. Ghazzal conceptualized and conceived the idea, acquired financing, supervised the work, contributed to the manuscript skeleton, and reviewed and edited the final manuscript. The manuscript was written with the help of all the co-authors.

Conflicts of interest

There are no conflicts to declare.

Acknowledgments

The authors thank the public grant overseen by the French National Research Agency (ANR) through the INGENCAT project (ANR-20-CE43-0014). V.D.Quach and M.N.Ghazzal appreciated Mrs. Audrey Gayral and Prof. Marie Erard (Institut de Chimie Physique, Université Paris-Saclay, CNRS UMR 8000, Orsay, France) for the access to TCSPC laser system. V.D.Quach acknowledges Ms. NGUYEN Thi-Ha-Xuyen (Centre d'Innovation Matériaux et Procédés, Institut Mines Telécom, Université de Lille, Lille, France) for the assistance of fitting open-circuit voltage decay by Matlab processing. ICN2 acknowledges funding from Generalitat de Catalunya 2021SGR00457. This study is part of the Advanced Materials program and was supported by MCIN with funding from European Union NextGenerationEU (PRTR-C17.I1) and by Generalitat de Catalunya. The authors thank the support from the project NANOGEN (PID2020-116093RB-C43), funded by MCIN/ AEI/10.13039/501100011033/ and by "ERDF A way of making Europe," by the "European Union." ICN2 is supported by the Severo Ochoa program from Spanish MCIN / AEI (Grant No.: CEX2021-001214-S) and is funded by the CERCA Programme / Generalitat de Catalunya. Part of the present work has been performed in the Universitat Autònoma de Barcelona Materials Science PhD program framework. M.Botifoll acknowledges support from SUR Generalitat de Catalunya and the EU Social Fund; project ref. 2020 FI 00103. ICN2 is founding member of e-DREAM.[64]

References

1 Z. Li, W. Luo, M. Zhang, J. Feng and Z. Zou, *Energy and Environmental Science*, 2013, **6**, 347–370.
2 S. J. A. Moniz, S. A. Shevlin, D. J. Martin, Z.-X. Guo and J. Tang, *Energy and Environmental Science*, 2015, **8**, 731–759.
3 J. Jia, L. C. Seitz, J. D. Benck, Y. Huo, Y. Chen, J. W. D. Ng, T. Bilir, J. S. Harris and T. F. Jaramillo, *Nature Communications*, 2016, **7**, 13237.
4 H. Nishiyama, T. Yamada, M. Nakabayashi, Y. Maehara, M. Yamaguchi, Y. Kuromiya, Y. Nagatsuma, H. Tokudome, S. Akiyama, T. Watanabe, R. Narushima, S. Okunaka, N. Shibata, T. Takata, T. Hisatomi and K. Domen, *Nature*, 2021, **598**, 304–307.
5 A. Fujishima and K. Honda, *Nature*, 1972, **238**, 37–38.
6 G. D. Gesesse, C. Wang, B. K. Chang, S.-H. Tai, P. Beaunier, R. Wojcieszak, H. Remita, C. Colbeau-Justin and M. N. Ghazzal, *Nanoscale*, 2020, **12**, 7011–7023.
7 X. Sun, S. Jiang, H. Huang, H. Li, B. Jia and T. Ma, *Angew Chem Int Ed*, 2022, **61**, e202204880.
8 Y. Liu, C. Zhang, J. Feng, X. Wang, Z. Ding, L. He, Q. Zhang, J. Chen and Y. Yin, *Angew Chem Int Ed*, 2023, **62**, e202308930.
9 L. Guo, Z. Yang, K. Marcus, Z. Li, B. Luo, L. Zhou, X. Wang, Y. Du and Y. Yang, *Energy and Environmental Science*, 2018, **11**, 106–114.
10 M. A. Rahman, S. Bazargan, S. Srivastava, X. Wang, M. Abd-Ellah, J. P. Thomas, N. F. Heinig, D. Pradhan and K. T. Leung, *Energy and Environmental Science*, 2015, **8**, 3363–3373.
11 J. Li, A. Slassi, X. Han, D. Cornil, M. Ha-Thi, T. Pino, D. P. Debecker, C. Colbeau-Justin, J. Arbiol, J. Cornil and M. N. Ghazzal, *Advanced Functional Materials*, 2021, **31**, DOI:10.1002/adfm.202100994.
12 C. Wang, J. Li, E. Paineau, H. Remita and M. N. Ghazzal, *Solar RRL*, 2023, **7**, DOI:10.1002/solr.202200929.
13 A. Wang, J. Li and T. Zhang, *Nature Reviews Chemistry*, 2018, **2**, 65–81.
14 L. Piccolo, P. Afanasiev, F. Morfin, T. Len, C. Dessal, J. L. Rousset, M. Aouine, F. Bourgain, A. Aguilar-Tapia, O. Proux, Y. Chen, L. Soler and J. Llorca, *ACS Catalysis*, 2020, **10**, 12696–12705.
15 T. W. van Deelen, C. Hernández Mejía and K. P. de Jong, *Nature Catalysis*, 2019, **2**, 955–970.
16 S. J. Tauster, S. C. Fung, R. T. K. Baker and J. A. Horsley, *Science*, 1981, **211**, 1121–1125.
17 V.-D. Quach, R. Wojcieszak and M. N. Ghazzal, *ChemNanoMat*, 2023, **9**, DOI:10.1002/cnma.202300329.
18 C. Gao, J. Low, R. Long, T. Kong, J. Zhu and Y. Xiong, *Chemical Reviews*, 2020, **120**, 12175–12216.
19 G. Pacchioni and H.-J. Freund, *Chemical Society Reviews*, 2018, **47**, 8474–8502.
20 S. Rhatigan and M. Nolan, *Journal of Materials Chemistry A*, 2018, **6**, 9139–9152.
21 M. Li, T. Zhang, S.-Z. Yang, Y. Sun, J. Zhang, F. Polo-Garzon, K. M. Siniard, X. Yu, Z. Wu, D. M. Driscoll, A. S. Ivanov, H. Chen, Z. Yang and S. Dai, *ACS Catalysis*, 2023, **13**, 6114–6125.
22 F. Polo-Garzon, T. F. Blum, V. Fung, Z. Bao, H. Chen, Z. Huang, S. M. Mahurin, S. Dai, M. Chi and Z. Wu, *ACS Catalysis*, 2020, **10**, 8515–8523.
23 H. Tang, Y. Su, B. Zhang, A. F. Lee, M. A. Isaacs, K. Wilson, L. Li, Y. Ren, J. Huang and M. Haruta, *Science Advances*, 2017, **3**, e1700231.
24 S. Liu, H. Qi, J. Zhou, W. Xu, Y. Niu, B. Zhang, Y. Zhao, W. Liu, Z. Ao, Z. Kuang, L. Li, M. Wang and J. Wang, *ACS Catalysis*, 2021, **11**, 6081–6090.

Open Access Article. Published on 10 June 2024. Downloaded on 6/11/2024 10:14:32 AM.
This article is licensed under a Creative Commons Attribution-NonCommercial 3.0 Unported Licence.

Journal of Materials Chemistry A Accepted Manuscript

This journal is © The Royal Society of Chemistry 20xx

Please do not adjust margins

View Article Online
DOI: 10.1039/D4TA03072A

25 R. Belgamwar, R. Verma, T. Das, S. Chakraborty, P. Sarawade and V. Polshettiwar, *Journal of the American Chemical Society*, 2023, **145**, 8634–8646.
26 C. Zhang, L. Wang, U. J. Etim, Y. Song, O. M. Gazit and Z. Zhong, *Journal of Catalysis*, 2022, **413**, 284–296.
27 J. Yu, X. Sun, X. Tong, J. Zhang, J. Li, S. Li, Y. Liu, N. Tsubaki, T. Abe and J. Sun, *Nat. Comm.*, 2021, **12**, 7209.
28 W. Levason and M. D. Spicer, *Coordination Chemistry Reviews*, 1987, **76**, 45–120.
29 M. Janczarek, Z. Wei, M. Endo, B. Ohtani and E. Kowalska, *Journal of Photonics for Energy*, 2016, **7**, 012008.
30 S. J. A. Moniz and J. Tang, *ChemCatChem*, 2015, **7**, 1659–1667.
31 W. Tabis, Y. Li, M. L. Tacon, L. Braicovich, A. Kreyssig, M. Minola, G. Dellea, E. Weschke, M. J. Veit, M. Ramazanoglu, A. I. Goldman, T. Schmitt, G. Ghiringhelli, N. Barišić, M. K. Chan, C. J. Dorow, G. Yu, X. Zhao, B. Keimer and M. Greven, *Nature Communications*, 2014, **5**, 5875.
32 R. Zhang, G. Jiang, Q. Gao, X. Wang, Y. Wang, X. Xu, W. Yan and H. Shen, *Nanoscale*, 2021, **13**, 15937–15951.
33 F.-T. Cheng, Y.-D. Geng, Y.-X. Liu, X. Nie, X.-G. Zhang, Z.-L. Chen, L.-Q. Tang, L.-H. Wang, Y.-Z. You and L. Zhang, *Nanoscale Advances*, 2023, **5**, 3336–3347.
34 G. D. Gesesse, T. Le Neel, Z. Cui, G. Bachelier, H. Remita, C. Colbeau-Justin and M. N. Ghazzal, *Nanoscale*, 2018, **10**, 20140–20146.
35 I. Vishik, *Science*, 2020, **369**, 775–776.
36 G. Palmer, in *Oxidation and Phosphorylation*, ed. M. E. P. Ronald W. Estabrook, Academic Press, New York, 1967, vol. 10, pp. 594–609.
37 G. W. Brudvig, in *Biochemical Spectroscopy*, ed. Kenneth Sauer, Academic Press, New York, 1995, vol. 246, pp. 536–554.
38 W. R. Hagen, *Dalton Transactions*, 2006, 4415.
39 M. A. Halcrow, *Chemical Society Reviews*, 2013, **42**, 1784–1795.
40 N. Sakaguchi Miyamoto, R. Miyamoto, E. Giamello, T. Kurisaki and H. Wakita, *Research on Chemical Intermediates*, 2018, **44**, 4563–4575.
41 F. A. Taiwo, *Spectroscopy*, 2003, **17**, 53–63.
42 A. Jain, S. P. Ong, G. Hautier, W. Chen, W. D. Richards, S. Dacek, S. Cholia, D. Gunter, D. Skinner, G. Ceder and K. A. Persson, *APL Materials*, 2013, **1**, 011002.
43 B. Kozlevčar and P. Šegedin, *Croatica Chemica Acta*, 2008, **81**, 369–379.
44 J. A. Aramburu, A. Bhowmik, J. M. Garcia-Lastra, P. García-Fernández and M. Moreno, *The Journal of Physical Chemistry C*, 2019, **123**, 3088–3101.
45 A. V. Kucherov, J. L. Gerlock, H.-W. Jen and M. Shelef, *The Journal of Physical Chemistry*, 1994, **98**, 4892–4894.
46 F. Gao, E. D. Walter, E. M. Karp, J. Luo, R. G. Tonkyn, J. H. Kwak, J. Szanyi and C. H. F. Peden, *Journal of Catalysis*, 2013, **300**, 20–29.
47 M. C. Biesinger, L. W. M. Lau, A. R. Gerson and R. St. C. Smart, *Applied Surface Science*, 2010, **257**, 887–898.
48 C. Wang, J. Li, E. Paineau, A. Laachachi, C. Colbeau-Justin, H. Remita and M. N. Ghazzal, *Journal of Materials Chemistry A*, 2020, **8**, 10779–10786.
49 M. C. Biesinger, *Surface & Interface Analysis*, 2017, **49**, 1325–1334.
50 G. Li, N. M. Dimitrijevic, L. Chen, T. Rajh and K. A. Gray, *The Journal of Physical Chemistry C*, 2008, **112**, 19040–19044.
51 X. Qiu, M. Miyauchi, K. Sunada, M. Minoshima, M. Liu, Y. Lu, D. Li, Y. Shimodaira, Y. Hosogi, Y. Kuroda and K. Hashimoto, *ACS Nano*, 2012, **6**, 1609–1618.
52 J. Zhang, C. Y. Toe, P. Kumar, J. Scott and R. Amal, *Applied Catalysis B: Environmental*, 2023, **333**, 122765.
53 H. Chen, Z. Yang, X. Wang, F. Polo-Garzon, P. W. Halstenberg, T. Wang, X. Suo, S. Z. Yang, H. M. Meyer, Z. Wu and S. Dai, *Journal of the American Chemical Society*, 2021, **143**, 8521–8526.
54 M. N. Ghazzal, M. Joseph, H. Kebaili, J. De Coninck and E. M. Gaigneaux, *J. Mater. Chem.*, 2012, **22**, 22526.
55 H. Irie, S. Miura, K. Kamiya and K. Hashimoto, *Chemical Physics Letters*, 2008, **457**, 202–205.
56 B. Choudhury, M. Dey and A. Choudhury, *Appl Nanosci*, 2014, **4**, 499–506.
57 J. Tauc, R. Grigorovici and A. Vancu, *physica status solidi (b)*, 1966, **15**, 627–637.
58 C. Dette, M. A. Pérez-Osorio, C. S. Kley, P. Punke, C. E. Patrick, P. Jacobson, F. Giustino, S. J. Jung and K. Kern, *Nano Letters*, 2014, **14**, 6533–6538.
59 D. O. Scanlon, C. W. Dunnill, J. Buckeridge, S. A. Shevlin, A. J. Logsdail, S. M. Woodley, C. R. A. Catlow, Michael. J. Powell, R. G. Palgrave, I. P. Parkin, G. W. Watson, T. W. Keal, P. Sherwood, A. Walsh and A. A. Sokol, *Nature Materials*, 2013, **12**, 798–801.
60 G. Wang, H. Wang, Y. Ling, Y. Tang, X. Yang, R. C. Fitzmorris, C. Wang, J. Z. Zhang and Y. Li, *Nano Letters*, 2011, **11**, 3026–3033.
61 C. Colbeau-Justin, M. Kunst and D. Huguenin, *Journal of Materials Science*, 2003, **38**, 2429–2437.
62 A. Zaban, M. Greenshtein and J. Bisquert, *ChemPhysChem*, 2003, **4**, 859–864.
63 W. Stöber, A. Fink and E. Bohn, *Journal of Colloid and Interface Science*, 1968, **26**, 62–69.
64 R. Ciancio, R. E. Dunin-Borkowski, E. Snoeck, M. Kociak, R. Holmestad, J. Verbeeck, A. I. Kirkland, G. Kothleitner and J. Arbiol, *Microscopy and Microanalysis*, 2022, **28**, 2900–2902.

Open Access Article. Published on 10 June 2024. Downloaded on 6/11/2024 10:14:32 AM.
This article is licensed under a Creative Commons Attribution-NonCommercial 3.0 Unported Licence.

Journal of Materials Chemistry A Accepted Manuscript

Please do not adjust margins

View Article Online
DOI: 10.1039/D4TA03072A

The data that support the findings of this study are openly available in https://zenodo.org/ at http://doi.org/**10.5281/zenodo.11489226**.

Open Access Article. Published on 10 June 2024. Downloaded on 6/11/2024 10:14:32 AM.
This article is licensed under a Creative Commons Attribution-NonCommercial 3.0 Unported Licence.

Journal of Materials Chemistry A Accepted Manuscript